



Snell's Law Applied to Tsunamis: Simulations and Observations

EMILE A. OKAL¹

Abstract—At the edge of a continental shelf, where the depth of the ocean column can vary rapidly by a factor of ~ 20 , tsunamis are expected to be severely refracted in application of Snell's Law. We use beaming techniques applied to numerical simulations under the shallow-water approximation, in the geometry of two real-life provinces of the Pacific Basin featuring sharp bathymetric discontinuities and extended shelves (Southeastern Alaska and Nicaragua). We conclude that tsunamis do indeed undergo refraction under Snell's Law with equivalent refraction indices as high as 5. We apply the same technique to actual records of the 2011 Tohoku tsunami by an array of seafloor pressure sensors off the coast of Southern California, and similarly observe Snell refraction despite a smaller velocity contrast and the presence of a shelf with extremely irregular bathymetry. Finally, we show numerically that for a source and a linear array of receivers both deployed on a well developed continental shelf bordering a deep basin, the tsunami will develop a head wave in all ways similar to the familiar case of refraction seismology.

Keywords: Tsunamis, Snell's Law, hydrodynamic simulations.

1. Introduction

The purpose of this paper is to explore conditions under which the interaction of tsunamis with sharp bathymetric discontinuities, such as the edge of a continental shelf, proceeds as a refraction obeying Snell's Law.¹

¹ Snell's Law takes its name from the Dutch mathematician Snellius (1621), but is known in French-speaking countries as Loi de Descartes, since it was stated in an appendix to the French philosopher's *Discours de la Méthode* in 1637. A longstanding controversy regarding the knowledge of Snell's work by R. Descartes, who was living in the Netherlands at the time, was never fully resolved (Kwan et al., 2002). At any rate, the geometry of

It has long been known that the propagation of tsunamis over deep water is controlled by the depth h of the ocean column, with the dispersion equation relating angular frequency ω to wavenumber k taking the general form

$$\omega^2 = gk \tanh(kh) \quad (1)$$

where g is the acceleration of gravity. Under the shallow water approximation [SWA], i.e., when the wavelength ($2\pi/k$) is much greater than h , this reduces to the classic non-dispersed formula

$$C = U = \sqrt{gh} \quad (2)$$

where phase and group velocities $C = \omega/k$ and $U = d\omega/dk$ are identical and independent of ω .

Because the depth h of the ocean is laterally heterogeneous, the propagation of tsunamis takes place over a medium with a variable velocity, and is characterized by large scale focusing and defocusing. Such effects were hinted at more than 60 years ago by Miyoshi (1955) and later modeled in more detail by Woods and Okal (1987) and Satake (1988). A spectacular application of the concept occurred during the great Sumatra–Andaman tsunami of 2004, when the Southwest Indian Ocean Ridge acted as a low-velocity waveguide trapping tsunami energy and delivering it into the Atlantic Ocean and eventually, through the Drake Passage, into the Pacific Ocean, reaching Hawaii 31.5 h after origin time (Okal, 2007; Titov et al., 2005).

The above studies were generally based on ray-tracing techniques developed to model the

Footnote 1 continued

refraction was already described in 984 A.D., i.e., 650 years earlier, by A. Ibn Sahl, a Persian scholar living in Baghdad, who was probably himself inspired by early but fragmentary work by Ptolemy, dating back to the second century A.D. (Rashed, 1990). In this paper, we will stick with the traditional name of “Snell's Law”.

¹ Department of Earth and Planetary Sciences, Northwestern University, Evanston, IL 60208, USA. E-mail: emile@earth.northwestern.edu

propagation of seismic surface waves in mildly heterogeneous media, for which the gradient of phase velocity remains smaller than the wave's frequency (e.g., Jobert & Jobert, 1983; Yomogida & Aki, 1985). In the present work, we will consider the opposite case of an abrupt change in velocity, occurring over a distance shorter than one wavelength. We are motivated by the situation at the edge of a continental shelf, where h can vary from a typical value of 4000 m in an abyssal plain to 200 m or less on the shelf, over a distance of 100 km or less. Under the SWA, this 20-fold decrease in depth implies a reduction of C by a factor of 4–5, predicting severe refraction effects. In the framework of geometrical optics, this would correspond to a refractive index $n = 4–5$, significantly larger than those of common transparent materials, diamond featuring one of the largest with $n = 2.65$.

Another significant difference with classical optics is the inverse dispersion expected in the case of tsunami waves. Whereas in light optics, the refractive index of a medium such as glass increases with frequency (with the well-known result that a prism deviates blue rays more than red ones), the opposite will be true for tsunamis: it can be shown from (1) that the derivative $\partial C / \partial h$ of phase velocity with respect to water depth is always positive, but also always remains a decreasing function of frequency. This simply expresses the fact that, as ω is increased outside the SWA, the wave no longer “feels” the bottom, and hence becomes insensitive to a change of depth.

These results are summarized on Fig. 1 which plots the refraction index $n = C_{Basin} / C_{Shelf}$, derived from Eq. (1), for various depth contrasts. For the more drastic case (4000 vs. 200 m, red curve on Fig. 1), n starts decreasing below 300 s, as the wave no longer follows the SWA in the basin but remains undispersed on the shelf. For a deeper slow medium (1000 m; green curve), the dispersion in n starts only around 200 s, as the wave has begun a slow dispersion, which compensates partially for that in the basin. Finally, for a transition between a shallow basin (1000 m) and a 200-m shelf, the dispersion in n remains negligible down to 100 s (blue curve), as the two media undergo only weak dispersion, practically compensating for each other.

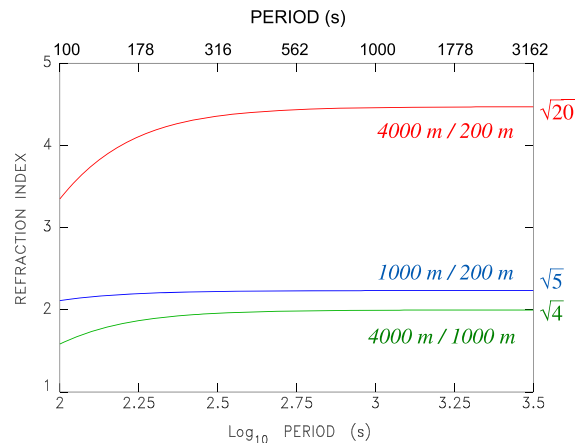


Figure 1

Dispersion of refraction indices n predicted by (1), at boundaries between a deep basin (4000 m), a shallow shelf (200 m), and a shallow basin (1000 m). The abscissa uses a logarithmic scale for period. Note the decrease of n with decreasing period, a dispersion opposite that of classical optics

For near-field tsunamis, the concept of the development of a head wave, both traveling faster and of a smaller amplitude than the regular one propagating in shallow water, emphasizes the fact that the fastest, first arrivals may not always be the largest, and serve only as harbingers of more destructive waves to follow. This picture has long been evidenced, understood, and repeated to populations at risk in the context of far-field tsunamis (Okal & Synolakis, 2016), but our results indicate a particular scenario under which it may become relevant even in the near field.

In addition, it is well-known in geometrical optics that refraction at a sharp interface is accompanied by reflection back into the incident medium, with an amplitude controlled by a combination of the index n and the angle of incidence. While such reflections have been observed in the case of tsunamis, their interpretation is made more complex by the fact that the change of depth responsible for the variation in velocity leads to a mechanical obstruction of part of the flow, notably its horizontal components, which carry most of the energy of the wave.

In this general context, (Rabinovich, 1993, Chap. 2.5) investigated theoretically the interaction of plane tsunami waves with various forms of continental shelf boundaries, using ray theory under the shallow water approximation, and derived resonant

conditions for the development of waves trapped along the shelf.

Our approach in this paper will be different, as we will focus both on virtual wavefields obtained from hydrodynamic simulations under the SWA and on one instance of actual recording of a teleseismic tsunami by an array of ocean-bottom hydrophones straddling the continental shelf off Southern California. In both instances, we will use a beam-forming methodology to define the parameters of propagation of the wave at it crosses the edge of the shelf.

2. Far-Field Simulations Under the Shallow-Water Approximation

In this section, we use numerical simulations under the shallow water approximation to evaluate the interaction of tsunamis with sharp continental shelf edges, using the actual bathymetry of the Pacific Ocean Basin. We single out for this experiment two regions characterized by well-developed, wide continental shelves and reasonably rectilinear boundaries between basin and shelf. Figure 2 details the bathymetry off the Alaska panhandle, where the shelf is approximately 100 km wide, and Fig. 3 off the coast of Nicaragua, where it extends for ~ 70 km. The azimuths of the shelf edges are taken as N302°E and N315°E, respectively.

2.1. Simulation Parameters

We set arrays of virtual gauges spanning the continental shelf, but avoiding areas of irregular bathymetry. On the Alaska shelf, we use 746 gauges with latitudinal and longitudinal steps of 3.8 km; the average water depth at the gauges is 168 ± 54 m. In the Alaska Basin, we use 966 gauges with the same separations, but at an average depth of 3213 ± 265 m. Off Nicaragua, we use 313 gauges on the shelf, at an average depth of 155 ± 92 m, and 594 gauges in the basin at an average depth of 3334 ± 673 m; the common step of the grids is 7.3 km. The corresponding average SWA celerities are listed in Table 1, and suggest refraction indices of 4.4 off Alaska and 4.9 off Nicaragua.

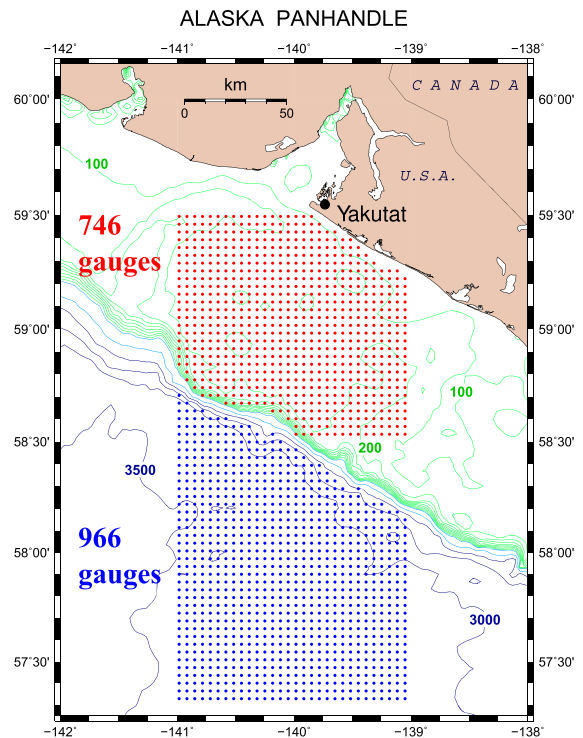


Figure 2

Map of the Alaskan virtual array. Bathymetry is contoured at 100-m intervals (in green) down to 1000 m, at 500-m intervals (in blue) deeper. The two subsets of shelf and basin virtual gauges are shown as red and blue dots, respectively

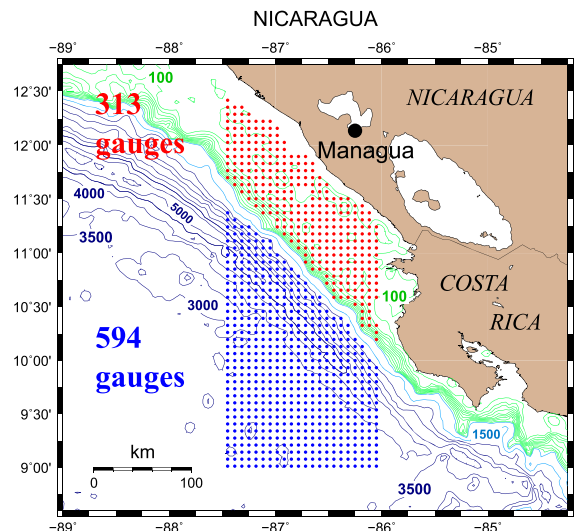


Figure 3

Same as Fig. 2 for the Nicaragua virtual array

Our simulations use the MOST algorithm (Titov & Synolakis, 1998; Titov et al., 2016), which is a

Table 1
Refraction parameters for the simulation experiments

Source-receiver pair	Tohoku–Alaska		Tohoku–Nicaragua		Iquique–Alaska		Iquique–Nicaragua	
	Basin	Shelf	Basin	Shelf	Basin	Shelf	Basin	Shelf
<i>Bathymetric parameters</i>								
Azimuth of shelf edge (N°E)	302		315		302		315	
Average SWA Velocity (m/s)	177 ± 8	40 ± 6	180 ± 19	37 ± 10	177 ± 8	40 ± 6	180 ± 19	37 ± 10
Predicted refraction index n	4.4		4.9		4.4		4.9	
Great Circle Back-Azimuth (N°E)	282	281	318	319	117	117	151	153
<i>Beaming results</i>								
Best beam C (m/s)	170	37	185	33	170	37	175	35
Best beam β (N°E)	239	218	292	235	176	204	166	216
Incidence i (N°E)	27	6	67	10	36	8	59	9
$n = \frac{C_B}{C_S}$	4.6		5.6		4.6		5.0	
$\frac{\sin i_B}{\sin i_S}$	4.3		5.3		4.2		5.5	

non-dispersive code under the SWA, solving the non-linear equations of hydrodynamics using the method of alternate steps (Godunov, 1959). MOST has been fully validated per international protocols (Synolakis, 2003; Synolakis et al., 2008). We consider two sources, modeled after the 2011 Tohoku and 2014 Iquique, Chile events, these geometries ensuring large incidence angles with respect to the shelf edges, in order to increase the effect of the refraction. Focal parameters for the earthquake sources are taken from the GlobalCMT catalogue (Dziewonski et al., 1981; Ekström et al., 2012). The significant difference in earthquake moment between the two cases is expected to result in different prominent wavelengths. We use Geller's (1976) scaling laws and Mansinha and Smylie's (1971) formalism to compute static solid-Earth displacements in the epicentral areas, which are then transposed as initial values of water elevation η for the simulations, a legitimate approximation for most realistic sources of large earthquakes (Derakhti et al., 2019). Simulations are carried out with a time step of 10 s, and a total duration of 95,000 s. A representative time series is shown on Fig. 4.

2.2. Beaming the Arrays

For each of the eight sets of simulations obtained, we proceed to beam the relevant arrays using a trial and error methodology. Specifically, we consider a set of time series $\eta_j(t)$, obtained at N virtual gauges indexed j , located at \mathbf{X}_j , with Cartesian coordinates E_j, N_j in an East–North frame centered at the centroid of the array. We assume that the tsunami sweeps the array with a slowness vector \mathbf{S} , of amplitude $S = 1/C$ and azimuth of arrival β , C being the phase velocity of the tsunami. This entices a delay at each station

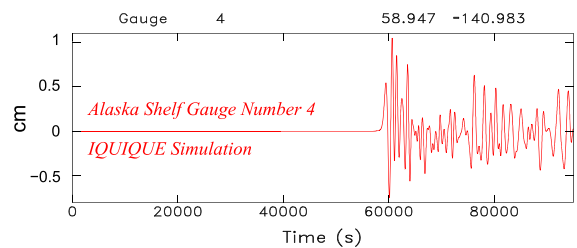


Figure 4
Time series $\eta(t)$ simulated at shelf virtual gauge number 4 (with coordinates listed in the header), representative of the simulation of the 2014 Iquique, Chile tsunami off the coast of Alaska. The time axis starts at the origin time of the earthquake

$$\tau_j = \mathbf{S} \cdot \mathbf{X}_j = -S(E_j \cos \beta + N_j \sin \beta) \quad (3)$$

We then stack the N time series at the gauges G_j after correcting for these delays

$$\eta^{Stack}(t) = \sum_{j=1}^N \eta_j(t - \tau_j) \quad (4)$$

When the chosen slowness \mathbf{S} is the actual one with which the simulated tsunami sweeps the array, the delayed time series are in phase and the amplitude of η^{Stack} is maximum.

Figures 5, 6, 7 and 8 show the results of a grid search on the parameters $C = 1/S$ and β for the 4 source-receiver combinations studied. For subarrays in oceanic basins, C is varied in 50 equal increments, between 50 and 300 m/s, and for the ones on shelves, between 25 and 125 m/s. The back-azimuth β is varied in 1° increments between 0 and 359° . The amplitude of the resulting stack is color-coded linearly using 12 tints between its maximum (red) and minimum (dark blue) values. The bull's eye symbol identifies the position of the maximum stacked amplitude, which defines the vector slowness \mathbf{S} of the simulated tsunami across the array. The black arrows across the diagrams represent the directions of the great circles between source and receiver. Finally, the small diagrams at the bottom center of each figure reproduce the inferred geometry of the refraction at the edge of the shelf. All relevant numbers are summarized in Table 1.

We first note that the directions of incidence of the waves in the basins deviate substantially (as much as 55°) from those of the great circles, since the latter would cross continental masses, or in the case of the Tohoku-Alaska path, the Bering Sea which is largely protected from penetration by the Aleutian Island chain. As expected, we verify that beamed phase velocities (170–185 m/s over the basins and 33–37 m/s over the shelves) are in excellent agreement with the SWA velocities averaged over the corresponding areas. Furthermore, we find that the angles of incidence computed from the beamed azimuths β and the strikes of the shelf edges verify Snell's law, with the refraction indices obtained from beamed slownesses and from the incident and refracted angles remaining within 10% of each other. Snell's law is

particularly well verified off Alaska where all such ratios are within 0.2 unit of the predicted index, $n = 4.4$ (Figs. 5, 6). The agreement remains good off Nicaragua, with beaming indices between 5.0 and 5.6, as compared with a predicted index of 4.9 (Figs. 7, 8).

3. Direct Observation of Tsunami Refraction: The 2011 Tohoku Event Recorded in the Los Angeles Basin

In this section, we apply the concept of Snell's Law to records of the 2011 Tohoku tsunami obtained from ocean-bottom pressure sensors during the ALBACORE Ocean-Bottom Seismometer [OBS] deployment off the coast of Southern California (Kohler et al., 2010, 2011).

In addition to their seismic channels, instrument packages deployed during OBS campaigns often include pressure sensors, but the latter are rarely used even though they are part of the datasets permanently archived at facilities such as the IRIS Data Management Center. In the case of ALBACORE, the sensors consisted of OBSIP-SIO/ABALONES- 4×4 gauges, recording at 50 samples per second, with an essentially flat response to pressure for $f > 3$ mHz, falling only as f at lower frequencies, thus keeping an adequate response at typical tsunami frequencies (as opposed for example to the SOFAR hydrophones suffering from severe high-pass filtering which prevented their quantitative use at the prominent tsunami frequencies during the 2004 Sumatra–Andaman earthquake (Okal et al., 2007)).

The ALBACORE deployment featured 34 ocean-bottom stations, split about evenly between 18 deep-water sites and 14 sites on the continental shelf (an additional two straddled the continental slope). The strike of the shelf slope is taken as $N315^\circ E$. By a stroke of luck, the 2011 Tohoku earthquake took place during the ALBACORE deployment (although the southwesternmost station in the deep basin was by then inoperative). We could not find another similar dataset of ocean-bottom pressure sensors straddling an abrupt change in bathymetry at the edge of a wide shelf and operative during any of the large tsunamis of the past 15 years.

TOHOKU to ALASKA

Estimated Azimuth of Slope: 302°

Basin

Shelf

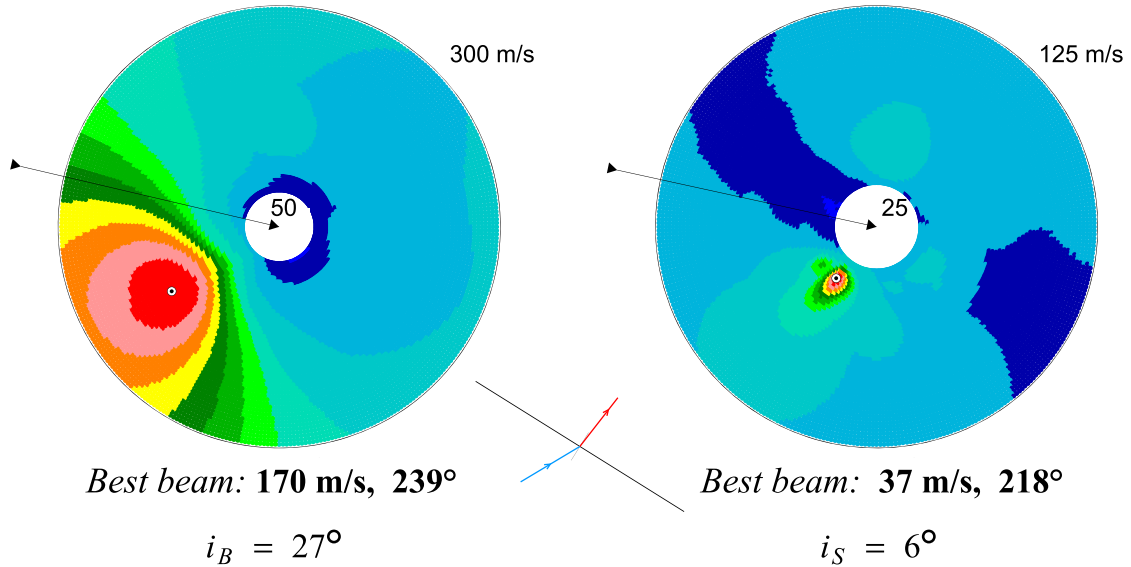


Figure 5

Beaming diagrams in the Tohoku-to-Alaska geometry at the basin (*Left*) and shelf (*Right*) arrays. For each slowness vector \mathbf{S} , the amplitude of the beam is color-coded at a point of radius $C = 1/S$ and at the back-azimuth of arrival β , with the scale of C printed at its minimum and maximum values. The color of the pixel varies as the amplitude of the resulting stack, linearly across 12 tints from maximum (red) to minimum (dark blue). The bull's eye symbols show the optimal beams, with Snell ratios summarized in the red box. The black arrows represent the directions of arrival of the source-receiver great circles at the centroids of the two subarrays. The diagram at bottom center represents the geometry of refraction for the optimal beam

Unfortunately, while the basin bathymetry is relatively smooth, the shelf has a tormented relief, and in particular is strewn with several shallow plateaux and even large islands (Fig. 9), thus rendering the propagation of the tsunami on the shelf extremely complex.

Records of the 2011 Tohoku tsunami at the ALBACORE ocean-bottom sites were used by Lin et al. (2015) to investigate the phase and group velocities of the tsunami across the array based on the eikonal equation, as applied for example to seismic surface waves by Lin et al. (2009). However, Lin

et al. (2015) did not investigate systematically the change in orientation of the wavefront as it transitions from deep to shallow water. We note also that most of the stations used by these authors belonged to the deep-water sub-array.

3.1. Numerical Simulations

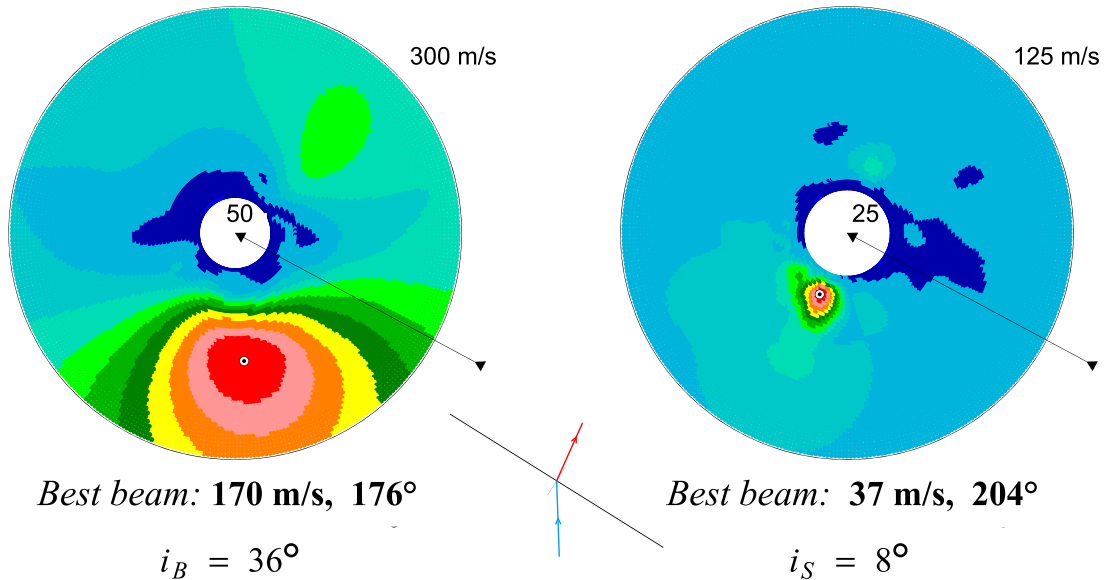
We start by repeating the experiment in Sect. 2 by simulating time series under the SWA using the MOST algorithm over dense grids of 855 and 297 virtual gauges, in the basin and shelf respectively,

IQUIQUE to ALASKA

Estimated Azimuth of Slope: 302°

Basin

Shelf



$$\frac{\sin i_B}{\sin i_S} = 4.2 \quad \frac{C_B}{C_S} = 4.6$$

Figure 6
Same as Fig. 5 for the Iquique-to-Alaska geometry

covering the general location of the ALBACORE experiment (Fig. 10). We obtain best beams featuring a phase velocity $C_B = 203$ m/s and a back azimuth $\beta_B = \text{N}297^\circ\text{E}$ in the basin, and $C_S = 76$ m/s; $\beta_S = \text{N}245^\circ\text{E}$ on the shelf (Fig. 11). The value of β_B is only 9° off that of the great circle which in this case remains far South of the continental boundaries of the Pacific Basin and of the Aleutian Islands; it translates into an incidence angle on the shelf slope $i_B = 72^\circ$, while its counterpart on the shelf yields $i_S = 20^\circ$. The Snell ratios then lead to comparable indices of refraction $(C_B/C_S) = 2.66$ and $(\sin i_B/\sin i_S) = 2.78$. This confirms that the tsunami wavefield simulated under the SWA indeed verifies Snell's Law.

In the deep basin, the beamed phase velocity corresponds to an SWA depth of 4200 m, in excellent agreement with the average depths at the 855 gauges. On the other hand, the value of C on the shelf corresponds to an average depth of 589 m, which is significantly shallower than the average at the 297 shallow gauges (948 m). This illustrates the extreme complexity of the shelf bathymetry off the coast of Southern California. It is probable that the tsunami wavefield remains coherent only over the shallower portions of the bathymetry, and those coherent signals then satisfy Snell's Law for the resulting slower velocities.

TOHOKU to NICARAGUA

Estimated Azimuth of Slope: 315°

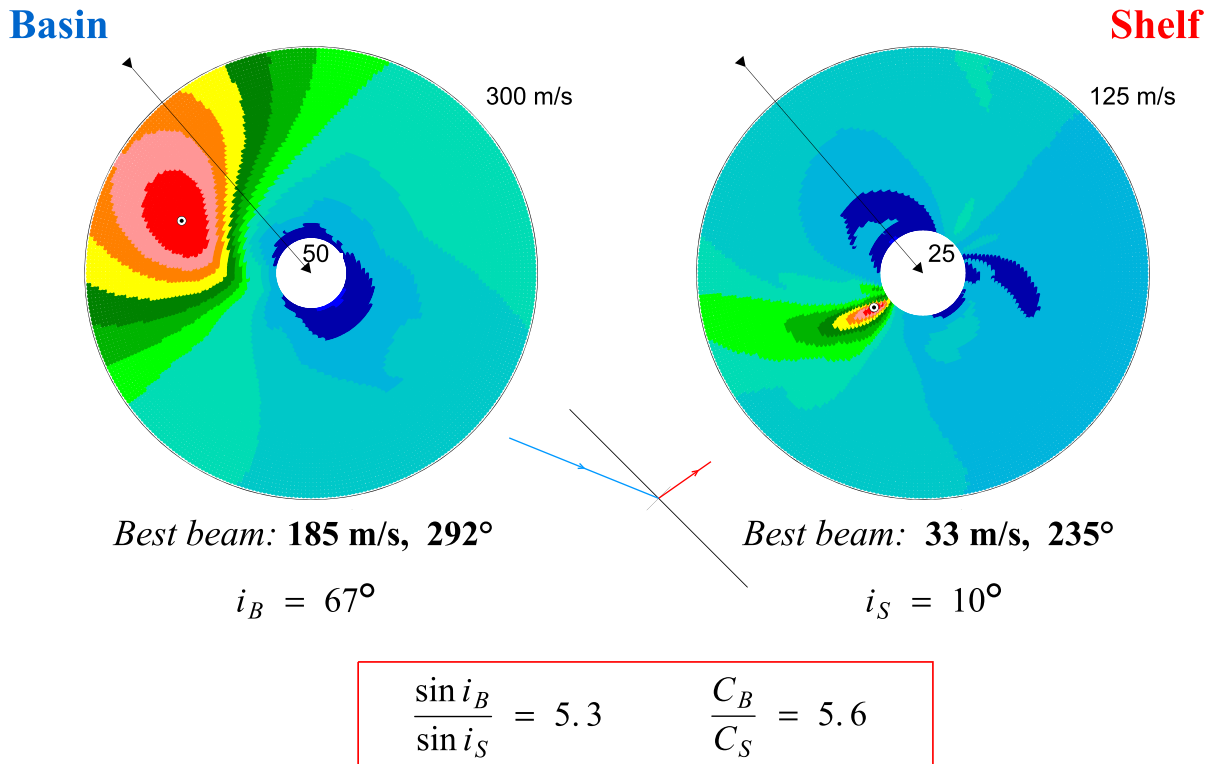


Figure 7

Same as Fig. 5 for the Tohoku-to-Nicaragua geometry

3.2. Beaming the Observed Data

We processed the ALBACORE data by first deconvolving the instrument response at each station, including the phase correction over and beyond the formal response listed in the IRIS data base, as documented by Lin et al. (2015). We then stacked the resulting records, filtered between 0.5 and 2 mHz, using the algorithm of Sect. 2. As shown on Fig. 12, we obtain for the 17-station basin subarray a best beam featuring a phase velocity $C_B = 200$ m/s with a back-azimuth $\beta_B = \text{N}290^\circ\text{E}$. For the 14-station shelf subarray, we similarly obtain beam parameters $C_S = 92$ m/s and $\beta_S = \text{N}252^\circ\text{E}$. The relevant incidence angles are then $i_B = 65^\circ$ and $i_S = 27^\circ$, and the Snell ratios $C_B/C_S = 2.12$ and $\sin i_B/\sin i_S = 2.06$. Their similarity indicates that

the low-frequency part of the tsunami wavefield indeed follows Snell's Law.

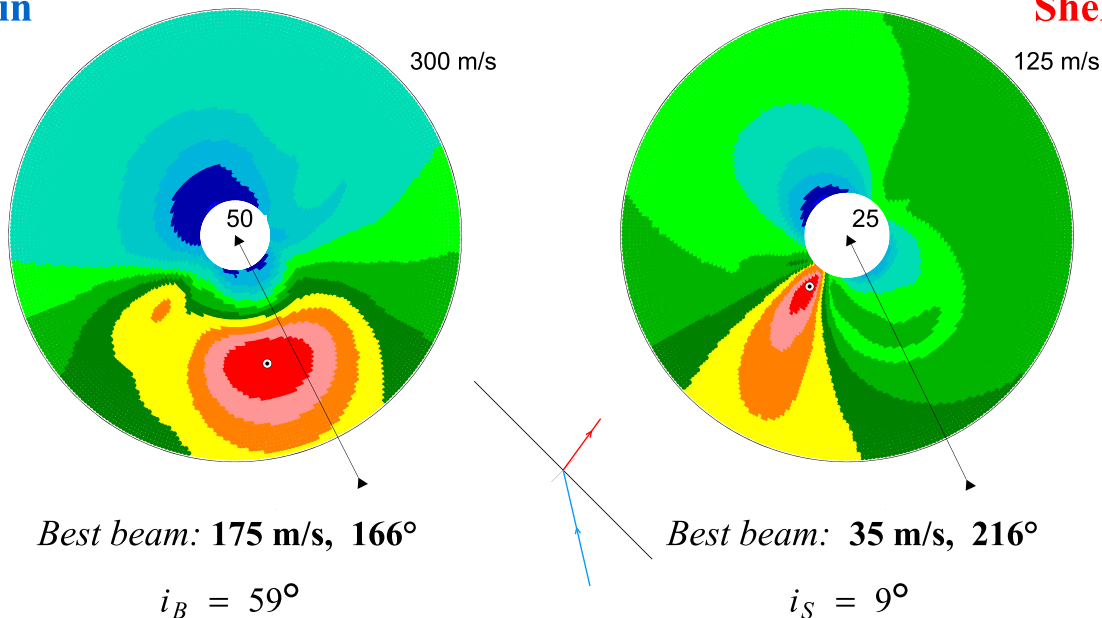
In the deep basin, the beamed velocity $C_B = 200$ m/s is in excellent agreement both with its counterpart from the SWA simulation (Sect. 3.1) and with Lin et al.'s (2015) results. It also agrees well with the average SWA velocities at the instrument sites (197 m/s). At the shelf sites, the beamed value ($C_S = 92$ m/s) is significantly larger than obtained from the simulation. We interpret this difference by suggesting that the irregular bathymetry and the islands present on the shelf modify the propagation of the longer wavelengths of the tsunami (i.e., its lower frequencies) and that the resulting field beams differently when sampled finely (as in our SWA simulation) or coarsely (as by the ALBACORE subarray).

IQUIQUE to NICARAGUA

Estimated Azimuth of Slope: 315°

Basin

Shelf



$$\frac{\sin i_B}{\sin i_S} = 5.5 \quad \frac{C_B}{C_S} = 5.0$$

Figure 8

Same as Fig. 5 for the Iquique-to-Nicaragua geometry

Finally, we attempted to repeat the above experiment at higher frequencies. A spectral examination of the available time series confirms the presence of energy, principally in the frequency bands 2.5–4.5 mHz and 4.5–7 mHz, having traveled across the Pacific outside the SWA, and thus arriving 5–11 h after the initial undispersed wavefront. In the deep basin, we were able to beam the array with best velocities $C_B = 194$ and 184 m/s and back azimuths $\beta_B = 285$ and 284° , in those two frequency bands respectively. The values of C_B are in good agreement with the values expected from (1) for a depth of 4 km and frequencies of 3 and 5 mHz, as well as with Lin et al.'s (2015) eikonal values. However, the same procedure failed to yield stable results for the subarray on the shelf. At the frequencies involved, the wavelengths in water 1000 m or less deep are 30

km or less at 3 mHz, and 15 km or less at 6 mHz. These are comparable to, if not smaller than, the typical coherence distances over which the extremely irregular bathymetry of the shelf varies, and unfortunately also the inter-station distances in the subarray, except for Stations 2–3 (26.5 km) and 27–28 (25.6 km). We thus surmise that the subarray is too coarse to adequately sample a coherent tsunami wave field at those frequencies.

4. A Simulated Experiment in “Tsunami Seismic Refraction”

In this section, we revert to the theoretical case of simulated waveforms, and investigate the possibility of generating a “head wave” comparable to those

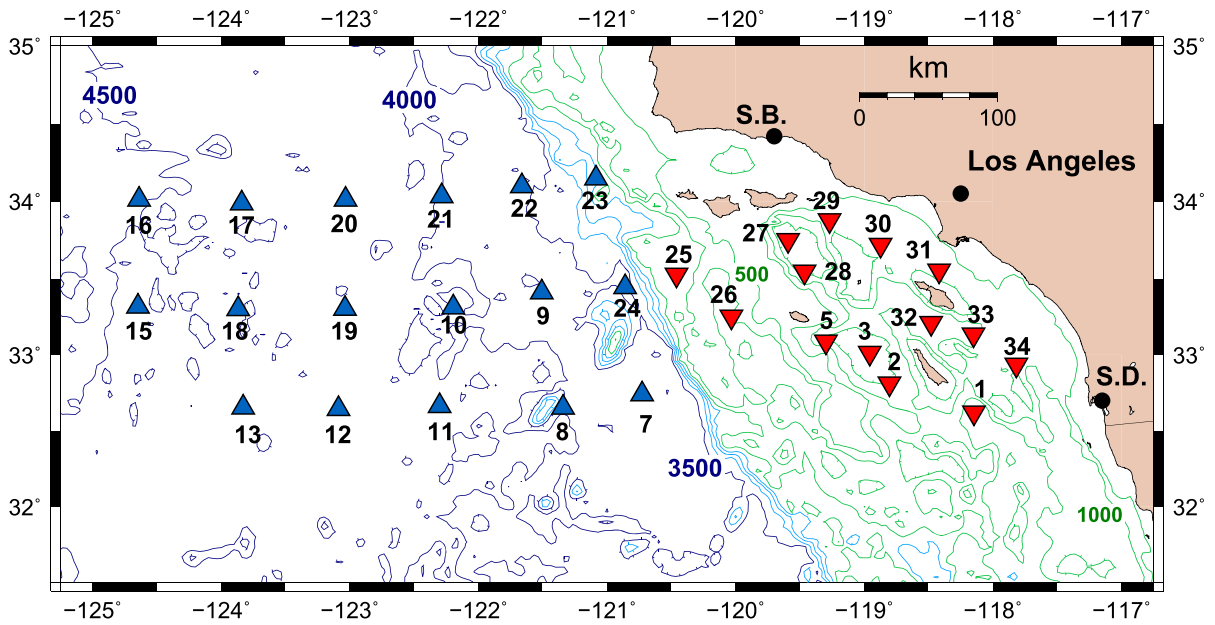


Figure 9

Map of the ALBACORE stations used in the present study. Deep-basin sites are shown as blue triangles, shelf ones as red inverted triangles. Numbers refer to station names (Lin et al., 2015). Isobaths are at 500-m intervals (green down to 1000 m, light blue to 3000 m, dark blue deeper). *S.B.* Santa Barbara, *S.D.* San Diego

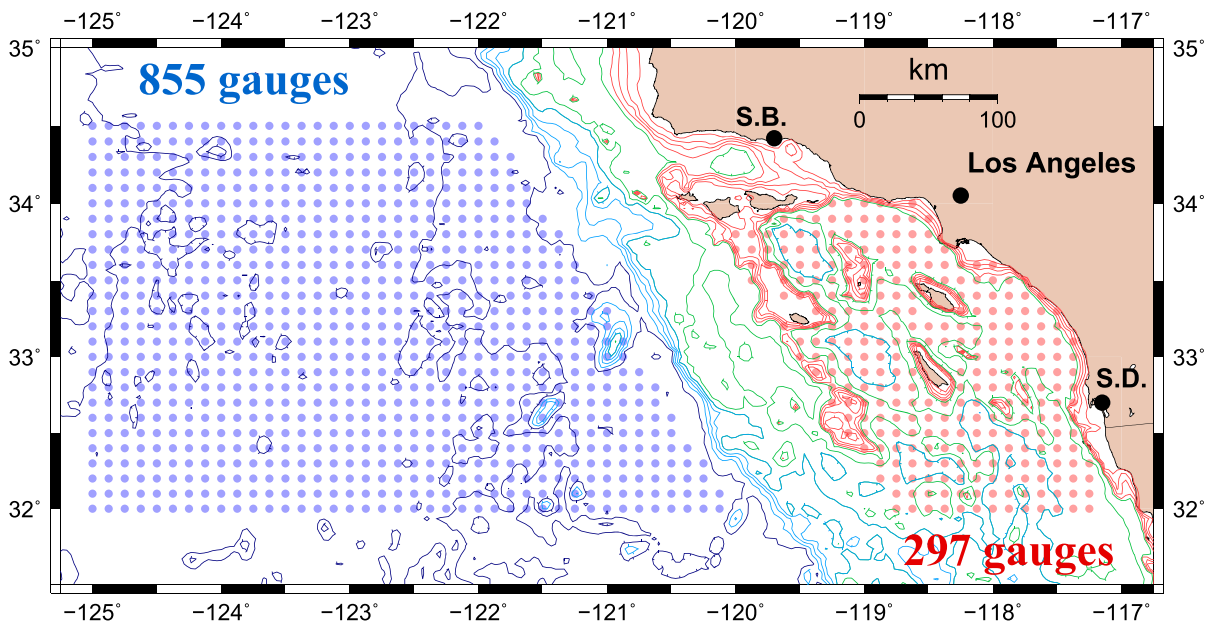


Figure 10

Map of the virtual arrays used for the simulation experiment in the ALBACORE area. In addition to the contours of Fig. 9, isobaths are shown in red at 100-m intervals (down to 400 m) to emphasize the presence of very shallow features on the shelf

2011 Simulations: Dense Grids

Estimated Azimuth of Slope: 315°

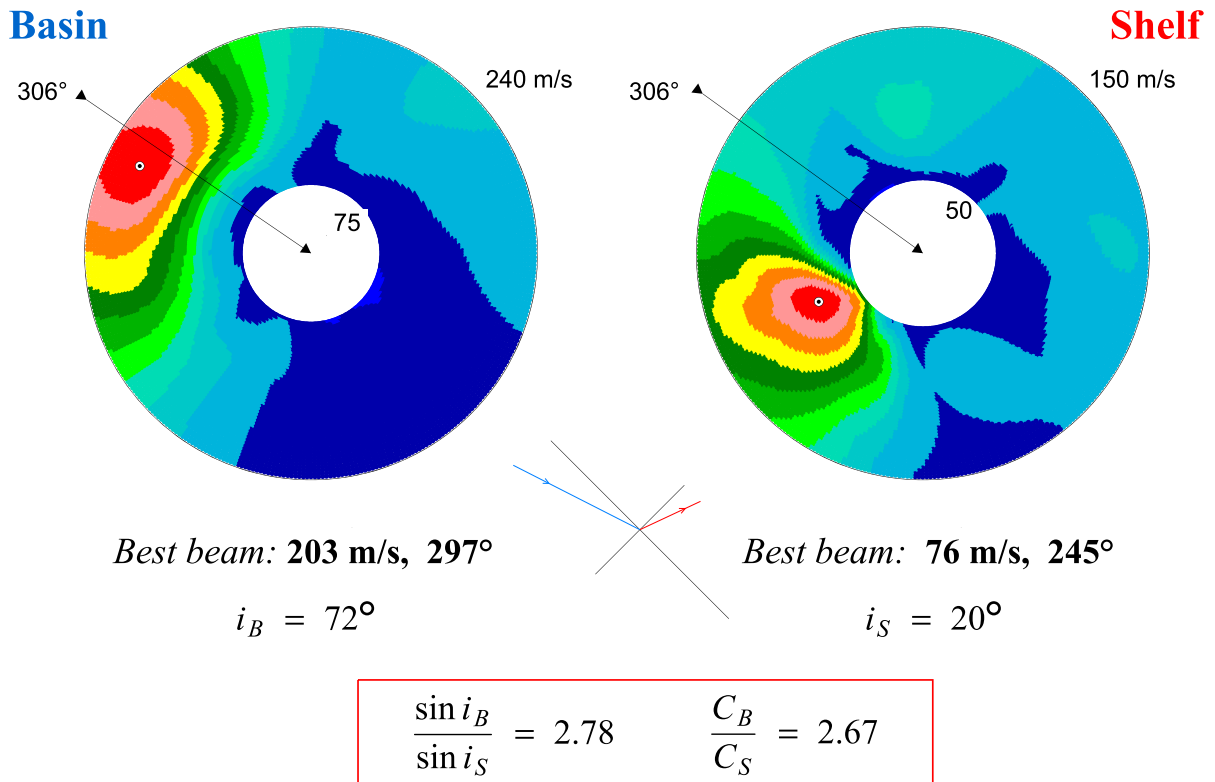


Figure 11

Results of the beaming experiment on the virtual gauges on Fig. 10. The time series have been filtered between 0.5 and 2 mHz, and processed with the same algorithms as for Fig. 5

used for exploration in seismic refraction experiments. We recall that the theory of the seismic head wave was first developed by Cagniard (1939), and later adapted by de Hoop (1960). A simple description of the phenomenon is that, for a sufficiently large distance, the fastest path between a source and a receiver both located in a slow layer overlying a faster half-space, is along a ray refracted into the half-space, and propagating below the boundary. This profile, mandated under Fermat's principle, is equivalent to the everyday experience of a motorist deviating from a straight-line path along city streets to take advantage of faster speeds on an admittedly distant expressway.

For this purpose, we return to the experiment off the Alaskan panhandle in Sect. 3, but we now consider a source on the shelf itself (59.5°N; 141.5°W) and a single linear array of 39 virtual receivers aligned with the source (Fig. 13a), at distances ranging from 7 to 175 km, along an azimuth paralleling the edge of the shelf (N302°E), this geometry mirroring that of a traditional seismic refraction experiment.

We consider a fault of length $L = 1$ km, width $W = 1$ km, and slip $\Delta u = 5$ m. This source does not satisfy seismic scaling laws, but it minimizes the effects of destructive interference due to finite source dimensions (Ben-Menahem & Rosenman, 1972). We use a fault geometry ($\phi = 302^\circ$; $\delta = 10^\circ$; $\lambda = 90^\circ$)

ALBACORE Data: 11 MAR 2011

Estimated Azimuth of Slope: 315°

15

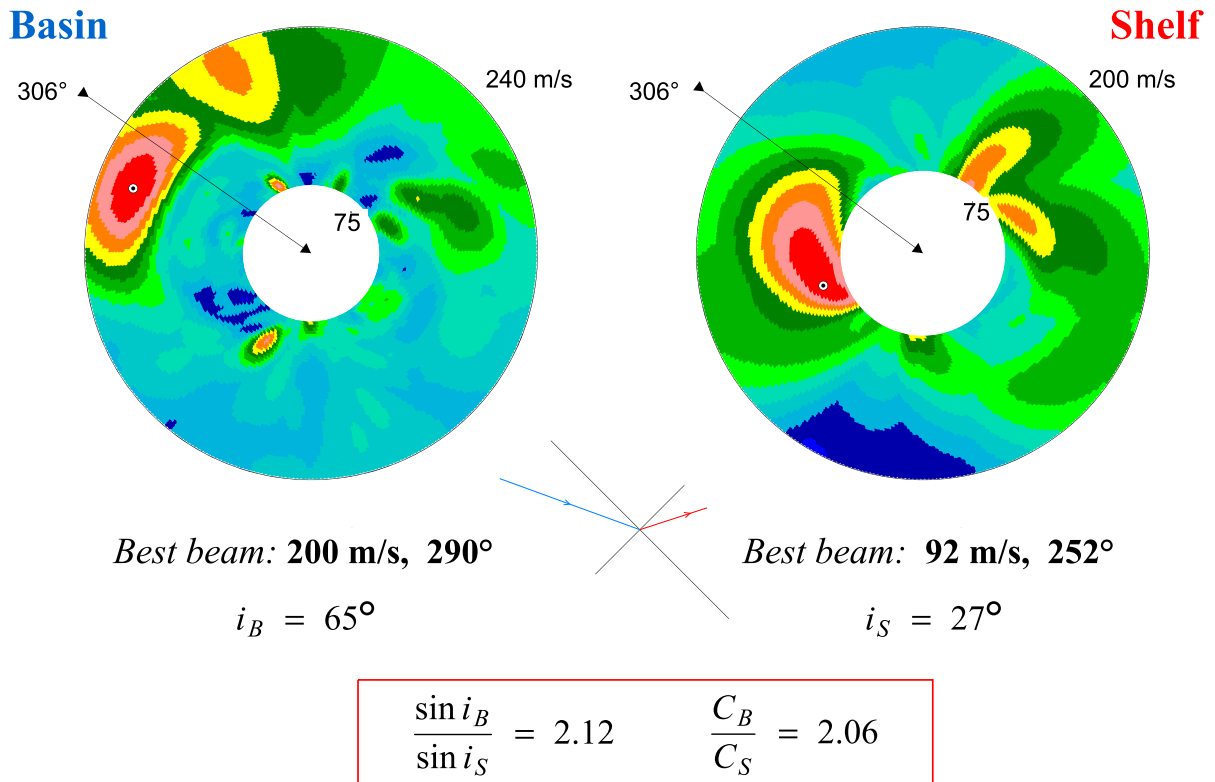


Figure 12

Results of the beaming experiment on the actual ALBACORE data (17 stations in the basin and 14 on the shelf). Details as in Fig. 5

expressing pure thrust on a shallow-dipping fault; once again, this source is not legitimate in the particular province where the motion between the Pacific and North American plates is mostly strike-slip, but our purpose is simply to conduct a virtual, theoretical experiment. We then run a numerical simulation using the MOST algorithm, for a time window lasting 9000 s.

The resulting time series at the 39 gauges are plotted on Fig. 13b in the form of a classic seismic refraction profile. Each trace is offset vertically by an amount proportional to the distance between source and receiver and is scaled to obtain common peak-to-peak amplitudes on the plot. It is clear that the first arrivals at short distances ($x \geq x_e = 102$ km) are well fit by a line of slowness $S_S = 23$ s/km, shown

on red on Fig. 13b. The slight deviations of the first arrivals from a straight line express local variations in depth, in particular as the profile crosses the Yakutat Canyon. At greater distances, a faster arrival develops, which can be fit with a slowness of only $S_B = 5.4$ s/km, shown in green on Fig. 13b.

The three parameters in the two-segment first-arrivals curve, i.e., the two slownesses S_S and S_B and the distance at the elbow x_e , are classically interpreted in terms of the structural parameters of the model, i.e., the two velocities and the thickness h of the layer, which in the present case will be the distance of the source-receiver line to the discontinuity:

$$V_S = 1 / S_S = 43 \text{ m/s}; \quad V_B = 1 / S_B = 185 \text{ m/s}$$

$$h = \frac{x_e}{2} \sqrt{\frac{S_S - S_B}{S_S + S_B}} = 40 \text{ km} . \tag{5}$$

The value of V_S corresponds to a depth of 189 m under the SWA, close to the average depth at the individual gauges (171 m). The difference with the value obtained on Fig. 5 ($C_S = 170 \text{ m/s}$) stems from the fact that the beaming procedure averages the field over the entire shelf, while the refraction experiment yields a slowness along the line of receivers. As for V_B , it corresponds to a depth of 3492 m, which is representative of a smooth, flat basin seawards of the shelf slope. Finally, the value of h is a reasonable estimate of the distance from the source to the abyssal plain.

An additional classic property of head waves is their emergent character, inherent in the behavior of

their Green's function as a growing ramp (Helmberger, 1968); as a result, head waves feature amplitudes generally lower than the direct waves at ranges immediately following the crossover distance x_e . While our simulated profile obviously lacks the resolution to explore this question in detail, the overall shape of the relevant waveforms (at the top of Fig. 13b) is generally supportive of such a behavior.

In conclusion, our simulation experiment shows that, under an appropriate geometry, the propagation of a tsunami on a continental shelf can lead to the development of a head wave in the nearby basin, in all respect similar to those encountered in seismic refraction, in particular the so-called P_n and S_n waves, controlled by the Mohorovičić discontinuity at the crust-mantle interface.

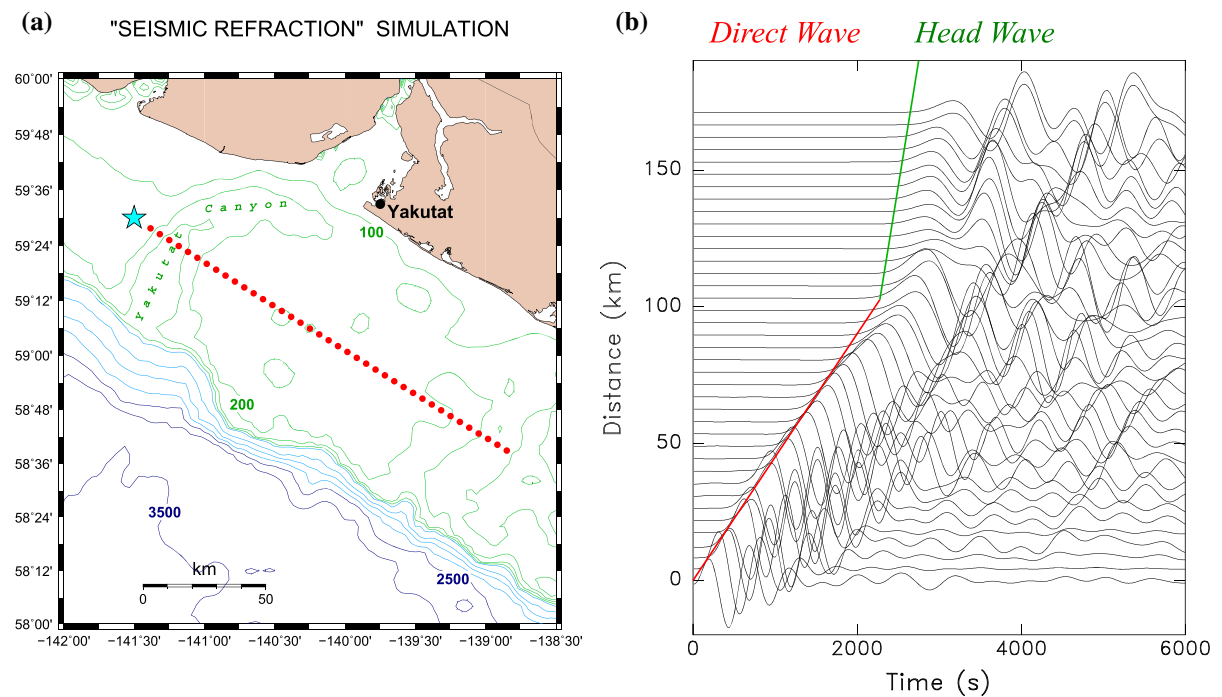


Figure 13

“Tsunami seismic refraction” experiment. **a** Map of the source (blue star) and of the 39 virtual gauge receivers, located on a line paralleling the edge of the shelf. **b** Time series profile. Each line represents the simulated amplitude $\eta(t)$, offset vertically according to the distance from the source to the respective virtual gauge. The peak-to-peak amplitude of each trace is scaled to a common value, in order to improve readability. The red line is a linear fit to the first arrivals at short distance, the green one identifies the head wave, which becomes the fastest arrival at the elbow $x_e = 102 \text{ km}$

5. Conclusion

Using numerical simulations and a remarkable but apparently single dataset of actual recordings by ocean-bottom pressure sensors, we have documented that teleseismic tsunami waves encountering severe discontinuities actually follow Snell's law, as expected from works such as Rabinovich's (1993), who investigated theoretically the conditions for resonant trapping of tsunami energy on the shelf. Unfortunately, as mentioned above, the only experimental array straddling a strong discontinuity operational during a major tsunami happened to be deployed off Southern California, whose extremely complex bathymetry strongly affected the interaction of the tsunami with the shelf, and restricted our study to its lowest frequencies. In this respect, the development of DONET and S-NET arrays off the coast of Japan (Mochizuki et al., 2016) may hold the promise of seminal observations during future transoceanic tsunamis, even though most of the sensors have been deployed in relatively deep water ($h > 500$ m), in order to optimize their response time in the context of efficient tsunami warning.

An important consequence of the strong refraction of teleseismic tsunami waves at continental shelves is that, at least in the geometry of a linear coastline, they can be expected to reach the shore at essentially normal incidence, regardless of their original back azimuth on the high seas. This remark should simplify the modeling of their "final mile" interaction with coastal structures and the ensuing mitigation.

Acknowledgements

I thank A. B. Rabinovich for pointing out his 1993 monograph. The data used in Sect. 3 were obtained from the IRIS Data Center. Maps were drawn using the GMT software (Wessel & Smith, 1991).

Publisher's Note Springer Nature remains neutral with regard to jurisdictional claims in published maps and institutional affiliations.

REFERENCES

- Ben-Menahem, A., & Rosenman, M. (1972). Amplitude patterns of tsunami waves from submarine earthquakes. *Journal of Geophysical Research*, *77*, 3097–3128.
- Cagniard, L. (1939). *Réflexion et réfraction des ondes sismiques progressives* (260 p.). Gauthier-Villars.
- de Hoop, A. T. (1960). A modification of Cagniard's method for solving seismic pulse problems. *Applied Science Research*, *B8*, 349–356.
- Derakhiti, M., Dalrymple, R. A., Okal, E. A., & Synolakis, C. E. (2019). Temporal and topographic source effects in tsunami generation. *Journal of Geophysical Research Oceans*, *124*, 5270–5288.
- Dziewonski, A. M., Chou, T.-A., & Woodhouse, J. H. (1981). Determination of earthquake source parameters from waveform data for studies of global and regional seismicity. *Journal of Geophysical Research*, *86*, 2825–2852.
- Ekström, G., Nettles, M., & Dziewonski, A. M. (2012). The GlobalCMT project, 2004–2010: Centroid-moment-tensors for 13017 earthquakes. *Physics of the Earth and Planetary Interiors*, *200*, 1–9.
- Geller, R. J. (1976). Scaling relations for earthquake source parameters and magnitudes. *Bulletin of the Seismological Society of America*, *66*, 1501–1523.
- Godunov, S. K. (1959). Finite difference methods for numerical computations of discontinuous solutions of the equations of fluid dynamics. *Matematicheskii Sbornik*, *47*, 271–295.
- Helmberger, D. V. (1968). The crust-mantle transition in the Bering Sea. *Bulletin of the Seismological Society of America*, *58*, 179–214.
- Jobert, N., & Jobert, G. (1983). An application of ray theory to the propagation of waves along a laterally heterogeneous spherical surface. *Geophysical Research Letters*, *10*, 1148–1151.
- Kohler, M., Weeraratne, D.S., Booth, K., Celnick, M., Cleary, E., Clements, B., Huang, L., Shintaku, N., Sun, C., Tsang, S., Zhu, J., Aaron, E., Thai, P., Gibaud, M., Kao, R., Flores, D., Anderson, D., Meyer, J. & Rowe, B. (2010). *ALBACORE OBS deployment cruise report* (27 p.). California Institute of Technology. <https://resolver.caltech.edu/CaltechAUTHORS:20160211-163227527>.
- Kohler, M., Weeraratne, D.S., Ahn, C., Brunner, K., Clements, B., Escobar, L., Logan, P., Sotirov, T., Zhu, J., Lambert, R., Mogk, S., Aaron, E., Gibaud, M., Thai, P., Anderson, D., & Donohue, M. (2011). *ALBACORE OBS recovery cruise report* (35 p.). California Institute of Technology. <https://resolver.caltech.edu/CaltechAUTHORS:20160211-162914168>.
- Kwan, A., Dudley, J., & Lantz, E. (2002). Who really discovered Snell's Law? *Physics World*, *15*, 64.
- Lin, F.-C., Ritzwoller, M. H., & Snieder, R. (2009). Eikonal tomography: Surface wave tomography by phase front tracking across a regional broad-band seismic array. *Geophysical Journal International*, *177*, 1091–1110.
- Lin, F.-C., Kohler, M. D., Lynett, P., Ayca, A., & Weeraratne, D. S. (2015). The 11 March 2011 Tohoku tsunami wavefront mapping across offshore Southern California. *Journal of Geophysical Research Solid Earth*, *120*, 3350–3362.
- Mansinha, L., & Smylie, D. E. (1971). The displacement fields of inclined faults. *Bulletin of the Seismological Society of America*, *61*, 1433–1440.

- Miyoshi, H. (1955). Directivity of the recent tsunamis. *Journal of the Oceanographic Society of Japan*, 11, 151–155.
- Mochizuki, M., Kanazawa, T., Uehira, K., Shimbo, T., Shiomi, K., Kunugi, T., et al. (2016). S-NET project: Construction of large scale seafloor observatory network for tsunamis and earthquakes in Japan. *EOS, Transactions of the American Geophysical Union*, 97(53), NH43B-1840 (**abstract**).
- Okal, E. A. (2007). Seismic records of the 2004 Sumatra and other tsunamis: A quantitative study. *Pure and Applied Geophysics*, 164, 325–353.
- Okal, E. A., & Synolakis, C. E. (2016). Sequencing of tsunami waves: Why the first wave is not always the largest. *Geophysical Journal International*, 204, 719–735.
- Okal, E. A., Talandier, J., & Reymond, D. (2007). Quantification of hydrophone records of the 2004 Sumatra tsunami. *Pure and Applied Geophysics*, 164, 309–323.
- Rabinovich, A. B. (1993). *Long ocean gravity waves: Trapping, resonance, leaking* (325 p.). Gidrometeoizdat (**in Russian**).
- Rashed, R. (1990). A pioneer in anaclastics: Ibn Sahl on burning mirrors and lenses. *Isis*, 81, 464–491.
- Satake, K. (1988). Effects of bathymetry on tsunami propagation: Application of ray tracing to tsunamis. *Pure and Applied Geophysics*, 126, 27–36.
- Synolakis, C. E. (2003). Tsunami and seiche. In W.-F. Chen & C. Scawthron (Eds.), *Earthquake engineering handbook* (pp. 9_1–9_90). CRC Press.
- Synolakis, C. E., Bernard, E. N., Titov, V. V., Kânoğlu, U., & González, F. I. (2008). Validation and verification of tsunami simulation models. *Pure and Applied Geophysics*, 165, 2197–2228.
- Titov, V. V., & Synolakis, C. E. (1998). Numerical modeling of tidal wave run-up. *Journal of Waterway, Port and Coastal Ocean Engineering*, 124, 157–171.
- Titov, V. V., Rabinovich, A. B., Mofjeld, H. O., Thomson, R. E., & González, F. I. (2005). The global reach of the 26 December 2004 Sumatra tsunami. *Science*, 309, 2045–2048.
- Titov, V. V., Kânoğlu, U., & Synolakis, C. E. (2016). Development of MOST for real-time tsunami forecasting. *Journal of Waterway, Port and Coastal Ocean Engineering*, 142(6), 03116004.
- Wessel, P., & Smith, W. H. F. (1991). Free software helps map and display data. *EOS, Transactions of the American Geophysical Union*, 72, 441 and 445–446.
- Woods, M. T., & Okal, E. A. (1987). Effect of variable bathymetry on the amplitude of teleseismic tsunamis: A ray-tracing experiment. *Geophysical Research Letters*, 14, 765–768.
- Yomogida, K., & Aki, K. (1985). Waveform synthesis of surface waves in a laterally heterogeneous Earth by the Gaussian beam method. *Journal of Geophysical Research*, 90, 7665–7688.

(Received January 31, 2021, revised March 10, 2021, accepted March 13, 2021, Published online April 28, 2021)